

# Thermal Transport Catastrophe and the Tokamak Edge Density Limit

**D. A. D'Ippolito and J. R. Myra**

*Lodestar Research Corporation, 2400 Central Avenue, Boulder, Colorado 80301*

February, 2006; revised: April, 2006  
(to be published in Physics of Plasmas)

---

DOE/ER/54392-33

LRC-06-107

---

**LODESTAR RESEARCH CORPORATION**

# Thermal transport catastrophe and the tokamak edge density limit\*

D. A. D'Ippolito<sup>†</sup> and J. R. Myra

*Lodestar Research Corporation, 2400 Central Avenue, Boulder, Colorado 80301*

## Abstract

Experiments on the Alcator C-Mod tokamak [Phys. Plasmas **1**, 1511 (1994)] have demonstrated the existence of a density limit which appears to be caused not by radiation, but by perpendicular heat convection in the scrape-off-layer (SOL). The present paper shows that the collisionality dependence of the blob model provides a plausible explanation for this convective density limit under certain conditions. The thermal equilibrium and stability of the SOL are studied in a two-point (midplane, divertor) model including perpendicular heat convection. A general scaling of the perpendicular heat flux  $q_{\perp}$  with temperature is used to derive conditions for the SOL thermal equilibrium to have two roots and a fold catastrophe associated with root merger. For the particular scaling of  $q_{\perp}$  given by a “disconnected” blob model, this equilibrium limit can be interpreted as a SOL density limit associated with X-point cooling in which the blob heat transport plays a role analogous to radiation in other theories.

PACS numbers: 52.25.Fi, 52.35.Ra, 52.55.Dy, 52.55.Rk , 52.55.Fa

<sup>†</sup>email: [dippolito@lodestar.com](mailto:dippolito@lodestar.com)

## I. Introduction

It is well-known that magnetic confinement experiments have an operational limit on the line-averaged core-plasma electron density  $n_e$ .<sup>1</sup> This limit is of great practical importance for a fusion reactor because the fusion reaction rate scales like  $n_e^2$ . The physical explanation of the density limit is not yet completely understood, nor is it known whether the same process occurs in all experiments. It is generally accepted that some density-dependent cooling process in the edge or scrape-off-layer (SOL) causes shrinkage of the edge current channel, leading to magnetohydrodynamic (MHD) instabilities and disruption as the safety factor profile  $q(r)$  evolves. An empirical relation which works for many experiments is the Greenwald density limit,  $n_e < n_G$ , where

$$n_G = \frac{I_p}{\pi a^2}, \quad (1)$$

$I_p$  is the total plasma current, and  $a$  is the minor radius of the toroidal plasma. Here, the units of  $I_p$ ,  $a$ , and  $n_G$  are MA, m, and  $10^{20} \text{ m}^{-3}$ . The success of this limit is somewhat mysterious because it is framed in terms of the average core density, but almost all the density limit theories are based on physics that depends on the edge or SOL density (and impurity densities when radiation is considered), none of which enter directly into this expression. A theoretical understanding of Eq. (1) is outside the scope of this paper. Instead, we assume that the edge cooling responsible for the Greenwald density limit is driven by thermal collapse of the SOL plasma and focus on the latter problem. Here, we derive a condition for an edge / SOL density limit, leaving its relation to the Greenwald limit for future work.

There is an extensive literature on experimental and theoretical studies of the density limit (DL), which has been reviewed recently in two excellent articles.<sup>1,2</sup> Here, we mention just a few papers that are relevant to the present work. All DL theories are built around a density-dependent edge cooling mechanism. Much of the density limit

literature is concerned with *radiation-driven* density limits; these papers investigate either global power balance or local edge power balance using various confinement scalings and including edge radiation from light impurity ions. Another class of theories invokes *turbulent transport-driven* density limits. One recent paper solved for thermal equilibrium of the core plasma including edge impurity radiation and a model of drift-resistive ballooning turbulent transport.<sup>3</sup> Other groups have used 3D turbulence codes to investigate density limits due to increased turbulent transport at high collisionality.<sup>4-6</sup> These papers are closely related to the present work, as we discuss below. Finally, other recent papers have studied two-point models of SOL and divertor power balance including impurity radiation, ionization and recycling at the divertor plates for high recycling plasmas<sup>7</sup> and a gas target model with the DL assumed to coincide with full detachment for ultra-high recycling plasmas.<sup>8</sup> Our approach is closely related to that of Borrass;<sup>7,8</sup> we interpret the DL as resulting from thermal collapse of the SOL and use a two-point SOL power balance model to explore the physics. However, in our case the primary cooling mechanism is assumed to be turbulent transport. The present paper complements earlier studies<sup>4-6</sup> of density limits associated with 3D turbulence by making the connection with turbulence-induced blob transport.

Our work is motivated by experiments on Alcator C-Mod<sup>9</sup> that imply the existence of a density limit due to turbulent *radial heat convection*.<sup>10,11</sup> At low densities ( $n_e \ll n_G$ ) on C-Mod, the SOL profiles have two distinct regions: near the separatrix, the profiles are determined by parallel transport and decay sharply, but farther out the cross-field transport dominates for both particles and energy, with the result that the density and pressure profiles are flat. The boundary between the two regions moves inward as  $n/n_G$  increases, and the ratio of the cross-field to parallel power flows just outside the separatrix,  $q_{\perp} A_{\perp} / q_{\parallel} A_{\parallel}$ , is found to increase with collisionality.<sup>1,10,11</sup> (Here,  $q_{\parallel}$  and  $q_{\perp}$  are the parallel and perpendicular heat fluxes and  $q \cdot A$  is the power.) This power ratio  $q_{\perp} A_{\perp} / q_{\parallel} A_{\parallel}$  is small at low density but exceeds unity as  $n/n_G \rightarrow 1$  [see Fig. 5 in Ref. 10 or

Fig. 25 in Ref. 1]. It was suggested<sup>1,10-12</sup> that the observed density limit could be related to the turbulent perpendicular heat convection and was caused by the unstable nature of the collisionality scaling of the perpendicular transport: lower SOL temperatures give higher collisionality and thus increased  $q_{\perp}$ , and the temperature drops further leading to a rapid cooling and thermal collapse of the SOL. The assumption of turbulence-driven transport is supported by data showing that the fluctuations levels of saturation current increase with average density on C-Mod<sup>10,11</sup> and other machines.<sup>13,14</sup> The present paper describes a convective transport mechanism which is consistent with this picture and derives the conditions under which a DL is obtained.

Some theoretical support of this idea was already provided by a series of 3D edge turbulence simulations using the BOUT code.<sup>6</sup> In these simulations, the turbulent fluctuation levels and transport increased strongly with collisionality, and at high edge density the perpendicular turbulent transport dominated the parallel classical transport, leading to divertor detachment. As the density limit was approached in these simulations, a transition was observed from resistive X-point mode turbulence to resistive ballooning turbulence. This transition was obtained more easily when the SOL was allowed to cool as the density was raised ( $p = nT = \text{const.}$ ). This work was qualitatively consistent with earlier simulations<sup>4,5</sup> and extended them in an important way by including the effect of the X-point geometry, and by investigating the effect of the enhanced cross-field transport on the equilibrium and thermal stability using the UEDGE code. The latter calculation showed that by diverting the heat flow away from the X-point, an X-point MARFE was triggered. (The acronym MARFE stands for “Multifaceted Asymmetric Radiation From the Edge”.)

In this paper, we describe a simple analytic model that is related to these experimental and simulation results. We consider SOL cooling by *turbulence-induced (blob) radial convection* for a diverted tokamak. We will show that the C-Mod experimental density-limit results and physical picture are consistent with the “blob”

model<sup>15,16</sup> of turbulent transport, extended to include the effects of parallel resistivity  $\eta_{\parallel} = (m_e v_e / 2ne^2)$  at the X-point.<sup>17-19</sup> Earlier work showed that the blob model gives good qualitative agreement with many aspects of the SOL transport observed in experiments.<sup>20</sup> The work described here extends this picture by showing that blobs which are electrically- and thermally-disconnected from the sheaths (and thus move more rapidly) can play a role analogous to that of radiation in cooling the X-point and triggering thermal collapse of the SOL.

In a sense, the thermal instability considered here is the convective analog to an X-point MARFE with the role of radiation replaced by cross-field blob heat transport. This idea is illustrated in Fig. 1. The SOL has two self-consistent thermal equilibrium states corresponding to different blob transport regimes. The first case has blobs which are connected to the sheaths and move outwards relatively slowly; parallel heat conduction is competitive with the radial heat transport, and the X-point remains hot, justifying the assumptions of thermal and electrical connection to the sheath. In the second state, the blobs are disconnected from the sheaths and therefore move faster;<sup>17-19</sup> the cross-field heat transport exceeds the parallel transport and the X-point cools, justifying the assumption of collisional disconnection from the sheath. One of the main results of this paper is to show that the latter state is thermally unstable, and the DL in this paper is associated with the transition from the connected to the disconnected state.

To produce a SOL density limit, the important physical properties of the blob model (see Sec. II B) are that both the blob generation rate (e.g. as seen in the simulations<sup>17</sup>) and the blob perpendicular velocity<sup>17-19</sup> increase with collisionality in the “disconnected blob” regime. The increase in blob velocity comes about because the blob current path becomes *electrically disconnected* from the sheaths as the collisionality  $\Lambda = (v_{ei} L_{\parallel} / \rho_s \Omega_e)$  increases [see Sec. II B]. This disconnection effect is enhanced by X-point geometry and influences the blob motion in the near SOL. The increase in blob transport with collisionality is also enhanced by *thermal disconnection* from the sheaths.

Sheath-connected blobs which are hotter than their surroundings develop a large Bohm sheath potential and tend to spin around their axis; rapid blob spin can reduce the charge polarization driving the radial motion.<sup>21</sup> As the collisionality increases, the blobs become thermally disconnected from the sheath, with the result that the spin disappears and the full charge polarization effect is obtained. The solution in Eq. (22) assumes no charge mixing by blob spin. Electrical disconnection implies thermal disconnection; both types of disconnection require  $\Lambda > \Lambda_{\text{crit}}$ , as discussed in Sec. II B.

Under certain conditions (derived in Sec. III A) the increase in blob transport with collisionality leads to a bifurcation of solutions for the SOL thermal equilibrium corresponding to the picture in Fig. 1: there is a *thermally stable* root in which the X-point remains hot and the blobs move relatively slowly, and a *thermally unstable* root in which the X-point cools and the rapid perpendicular heat transport due to the blobs causes the thermal equilibrium to collapse. Mathematically, the equilibrium limit occurs in our model by root merging at a critical density and temperature, yielding a classic fold catastrophe. Physically, the equilibrium passes from the stable to the unstable root at the critical (root merger) point. A similar situation also occurs in some models of radiation-driven collapse.<sup>22,2</sup> Thus, we will show that the blob transport drives a transport catastrophe associated with X-point cooling as the SOL density is raised.

There is experimental evidence to support the hypothesis that blob cross-field transport is associated with the density limit on C-Mod. Gas-puff imaging (GPI) measurements<sup>23</sup> on C-Mod yield two-dimensional movies of blob radial and poloidal motion in the SOL, and the associated radial convective transport by the blobs is the likely mechanism to explain the flat SOL profiles. Recent measurements show that the region in which blobs are born extends inside the separatrix for  $n/n_G > 0.6\text{--}0.7$ .<sup>24,25</sup> A more complete discussion of the experimental results is given in Sec. IV.

The observation of blob creation inside the separatrix at high collisionality can be understood as follows. In a highly collisional (resistive) plasma, the turbulence and blobs

have a strong ballooning structure at the midplane and are not affected very much by whether the end of the field line is closed, passes near an X-point or terminates in a sheath. In this limit, the SOL transport spills over into the edge as it cools, and the physics is the same just inside and outside the separatrix. This is likely the reason why the simulations of Refs. 5, 6 and the present model all give similar qualitative results as  $n/n_G \rightarrow 1$ .

The plan for this paper is as follows. Section II discusses the two-point SOL models for the time-evolution of the temperature (assuming fixed SOL densities) and for the blob transport. The SOL energy balance equations are solved by dimensional analysis in Sec. III for general scalings of the perpendicular convection on the midplane and X-point temperatures. A condition is derived for the existence of multiple roots (and the associated transport catastrophe) which has a simple physical interpretation in terms of X-point cooling. An analytic result is also obtained for the critical value of perpendicular convection. Finally, the connection of the equilibrium limits to thermal stability and to dynamical evolution is discussed. The relation of these results to the C-Mod experimental data is discussed in Sec. IV, and a summary and conclusions are given in Sec. V.

## **II. The Model**

### **A. Two-point SOL energy-balance model**

In this work, we have explored a number of models based on a “two-point” approximation along the field lines, representing the behavior of the plasma in the midplane and divertor regions. The complete model involves conservation equations for vorticity (charge), particle density  $n$  and electron temperature  $T = T_e$  in the SOL. For simplicity, we assume  $T_i \ll T_e$ . The starting point is the dimensional set of energy conservation equations in the two regions

$$\frac{3}{2} \frac{\partial(n_1 T_1)}{\partial t} = \frac{(q_{\perp \text{core}} - q_{\perp 1})}{L_{\perp}} - \frac{q_{12}}{L_1}, \quad (2)$$

$$\frac{3}{2} \frac{\partial(n_2 T_2)}{\partial t} = \frac{q_{12} - q_{23}}{L_2}, \quad (3)$$

where the subscripts 1 and 2 refer to the midplane and divertor regions, region 3 is the sheath, and double subscripts indicate the direction of parallel flow between the regions, e.g. 12 implies “from region 1 to region 2”, and  $L_j$  is the parallel scale length of region  $j$ . We retain parallel heat conduction and convection in  $q_{12}$ , and appropriate sheath BCs (in  $\Gamma_{23}$  and  $q_{23}$ ) to obtain the following parallel particle and heat fluxes

$$\Gamma_{12} = n_1 c_{s1}, \quad \Gamma_{23} = n_2 c_{s2}, \quad q_{23} = \gamma_{\text{sh}} \Gamma_{23} T_2, \quad (4)$$

$$\begin{aligned} q_{12} &= -\frac{\kappa_{12}}{L_{12}}(T_2 - T_1) + \alpha_{\parallel} \Gamma_{12} T_1, \\ &\approx \frac{\kappa_0}{L_{12}} T_2^{5/2} (T_1 - T_2) + \alpha_{\parallel} \Gamma_{12} T_1, \end{aligned} \quad (5)$$

where  $c_{sj} = (T_j/m_j)^{1/2}$  is the sound speed in region  $j$ ,  $\alpha_{\parallel}$  is the thermal convection coefficient, and  $\gamma_{\text{sh}}$  is the sheath energy transmission coefficient (typically,  $\alpha_{\parallel} = 5/2$  and  $\gamma_{\text{sh}} = 5$ ). Assuming that the thermal conductivity is dominated by the colder X-point / divertor region, its coefficient is defined by  $\kappa_{12} = 3.2 (n v_{\text{the}}^2) / v_e \equiv \kappa_0 T^{5/2}$  with  $T \rightarrow T_2$ . For  $T$  given in eV, the constant  $\kappa_0$  is given by  $\kappa_0 = 1.93 \cdot 10^{21} / \lambda_C \text{ cm}^{-1} \text{ s}^{-1} \text{ eV}^{-5/2}$ , where  $\lambda_C$  is the Coulomb logarithm. Here  $L_{12}$  is the parallel length of the transition region near the X-point.

The perpendicular heat flux from the core,  $q_{\perp \text{core}}$ , provides the heat source to the SOL and is assumed to be constant. The perpendicular heat loss from the SOL is assumed to be localized in the midplane ( $q_{\perp} = q_{\perp 1}$ ) and caused by blob convection. Thus, we express the perpendicular particle and heat fluxes as

$$\Gamma_{\perp 1} = f_b n_1 v_{\perp, \text{blob}}, \quad q_{\perp 1} = \Gamma_{\perp 1} T_1, \quad (6)$$

where  $f_b$  is the “packing fraction” of the blobs defined in Sec. II B, which is a measure of the blob creation rate. The blob velocity  $v_{\perp, \text{blob}}$  is proportional to  $\delta n_1/n_1$ , where  $\delta n$  is the height of the blob above the background density profile, because of the effect of the background density on the blob velocity, as seen in simulations.<sup>26,27</sup> In Sec. II B we will discuss the blob physics and parametric dependencies in more detail, and we will solve for the blob velocity in the disconnected blob limit assuming that  $f_b$  and  $\delta n_1/n_1$  are order unity. However, in carrying out the thermal equilibrium and stability analysis, it is useful to consider a general scaling of the blob velocity with temperatures, viz.

$$\Gamma_{\perp 1} = \Gamma_0 \frac{T_1^{\mu-1}}{T_2^{v/2}}, \quad q_{\perp 1} = \Gamma_0 \frac{T_1^{\mu}}{T_2^{v/2}}, \quad (7)$$

where  $\Gamma_0$  is a coefficient to be determined later. The motivation for this scaling will become apparent later in the paper, and it includes the disconnected blob solution in the 2-point model as a special case.

One can enlarge the model to include the continuity equations and attempt the ambitious goal of solving for densities and temperatures in both regions. We have carried out this solution but it is too complicated to illustrate the important points. Also, to obtain reasonable values of the densities one must include realistic SOL particle sources,  $S_{pj}$ , accounting for neutral recycling and ionization physics, in addition to the particle flux from the core (especially near the density limit). A simpler procedure is to turn the problem around and assume that the densities  $n_1$  and  $n_2$  are fixed in carrying out the thermal equilibrium and stability analysis. One then determines the required particle sources for equilibrium from the following continuity equations (with  $\partial n_j/\partial t = 0$ )

$$\frac{\partial n_1}{\partial t} = \frac{(\Gamma_{\perp \text{core}} - \Gamma_{\perp 1})}{L_{\perp}} - \frac{\Gamma_{12}}{L_1} + S_{p1}, \quad (8)$$

$$\frac{\partial n_2}{\partial t} = \frac{\Gamma_{12} - \Gamma_{23}}{L_2} + S_{p2} \quad . \quad (9)$$

Making use of these approximations, we can derive a set of dimensionless model equations for the thermal equilibrium and stability problems. To further simplify the equations, each term in the equation is normalized to the (assumed constant) core heat source  $q_{\perp\text{core}}(L_1/L_{\perp})$ , where  $q_{\perp\text{core}} = \Gamma_{\perp\text{core}} T_{\text{edge}}$ , and a reference SOL temperature  $T_r$  is defined such that the coefficient of the parallel thermal conductivity is unity in the dimensionless equations:

$$T_r = \left( \frac{q_{\perp\text{core}} L_{12} L_1}{\kappa_0 L_{\perp}} \right)^{2/7} \quad . \quad (10)$$

For typical C-Mod parameters,  $T_r$  is about 10-20 eV. The resulting equations for  $\bar{T}_j = T_j/T_r$  are

$$\tau_{E1} \frac{\partial \bar{T}_1}{\partial t} = 1 - C_{\perp} \frac{\bar{T}_1^{\mu}}{\bar{T}_2^{v/2}} - \bar{T}_2^{5/2} (\bar{T}_1 - \bar{T}_2) - C_{\parallel} \xi \bar{T}_1^{3/2} \equiv F_1(\bar{T}_1, \bar{T}_2), \quad (11)$$

$$\tau_{E2} \frac{L_2}{L_1} \frac{\partial \bar{T}_2}{\partial t} = \bar{T}_2^{5/2} (\bar{T}_1 - \bar{T}_2) + C_{\parallel} (\xi \bar{T}_1^{3/2} - \bar{T}_2^{3/2}) \equiv F_2(\bar{T}_1, \bar{T}_2). \quad (12)$$

For the remainder of this paper, unless otherwise noted, we drop the bars and let  $T_j$  denote the dimensionless temperature, and we assume  $L_1 = L_2$  for simplicity. Note that Eqs. (11) and (12) contain the effects of perpendicular convection (e.g. blob transport) through the  $C_{\perp}$  term, but omit radiation terms. Thus, our analysis is complementary to other density limit theories that focus on the effects of radiative cooling.

In these equations, the characteristic particle and energy transport time scales,  $\tau_{pj}$  and  $\tau_{Ej}$ , are defined as

$$\tau_{Ej} = \frac{3}{2} \frac{n_j L_{\perp}}{\Gamma_{\perp\text{core}}} \frac{T_r}{T_{\text{edge}}} = \tau_{pj} \frac{T_r}{T_{\text{edge}}} \quad , \quad (13)$$

so that  $\tau_E/\tau_p = (T_r/T_{\text{edge}})$ . The other transport coefficients are defined in terms of the heat fluxes at the reference temperature (i.e.  $T_1 = T_2 = T_r$ ) as

$$C_{\perp} = \frac{q_{\perp 1}|_{T_r}}{q_{\perp \text{core}}} , \quad C_{\parallel} = \frac{q_{23}|_{T_r}}{q_{\perp \text{core}}} \frac{L_{\perp}}{L_1} , \quad \xi \equiv \frac{\alpha_{\parallel}}{\gamma_{\text{sh}}} \frac{n_1}{n_2} . \quad (14)$$

For later use, we define dimensionless quantities proportional to the divergences of the perpendicular and parallel heat fluxes (normalized such that equilibrium energy balance has the form  $Q_{\perp} + Q_{\parallel} = 1$ ). These are given by

$$Q_{\perp} = C_{\perp} \frac{T_1^{\mu}}{T_2^{v/2}} , \quad Q_{\parallel} = C_{\parallel} T_2^{3/2} \quad (15)$$

and we also define the global SOL energy balance function  $F_{\text{SOL}}(T_1, T_2)$

$$\begin{aligned} F_{\text{SOL}}(T_1, T_2) &\equiv F_1 + F_2 = 1 - Q_{\perp} - Q_{\parallel} , \\ &= 1 - C_{\perp} \frac{T_1^{\mu}}{T_2^{v/2}} - C_{\parallel} T_2^{3/2} . \end{aligned} \quad (16)$$

## B. Blob transport physics

In this section, as motivation for the model just presented, we briefly review some relevant aspects of blob transport physics and derive a solution for the blob velocity in the two-point model. This particular solution is an important special case of the general scaling analyzed here.

The basic observation motivating the blob model is that edge turbulence in the highly nonlinear regime produces coherent structures with enhanced concentrations of density, temperature, and vorticity. These plasma ‘‘blobs’’ become charge-polarized because of the species-dependent curvature drift, and the resulting electric field causes an  $\mathbf{E} \times \mathbf{B}$  drift down the toroidal magnetic field gradient on the low field side of the torus.<sup>15,16</sup> By this mechanism, the  $\nabla B$  and toroidal curvature forces (or more generally, any outward radial force) can move the plasma towards the wall with a velocity of

typically  $v_x \sim 0.01 - 0.1 c_s$ . (The lower end of this range is found on C-Mod.) Recent work on three-dimensional (3D) blob models<sup>17-19</sup> has extended blob theory from the two-dimensional (2D) sheath-connected ballistic theory appropriate in the far SOL to the “resistive-X point” (RX) and “resistive ballooning” (RB) blob regimes appropriate in the near SOL and edge plasma, where the blobs are created by turbulence with a ballooning structure which is essential to the present work.

The blob dynamics can be thought of as controlled by an effective “electrical circuit”. The blob charge polarization is determined by balancing a fixed perpendicular current source (curvature-drift-induced current) with the parallel currents along the field lines. The blob charge and current densities have a dipole structure in the (approximately poloidal) direction perpendicular to its motion, giving a complete current path. The effective resistance along this path determines the voltage (the induced blob potential), which controls the strength of the blob  $\mathbf{E} \times \mathbf{B}$  velocity.<sup>17-19</sup> Depending on the parameter regime, there are several possible current paths, each giving a different scaling of blob velocity with the plasma parameters and each corresponding to a particular underlying linear instability.<sup>19</sup> The regime of interest in the present paper is the “disconnected” blob regime corresponding to the electrostatic RX instability,<sup>28</sup> in which the current loop is closed by perpendicular polarization drift currents across the thin elliptically-fanned part of the blob flux tube near the X-points.<sup>29</sup> This is the relevant blob regime when cooling (e.g. by gas puffing near the X-point) increases the parallel resistivity in the divertor region. Blobs with this scaling have been observed in 3D BOUT simulations of SOL turbulence in the high-density, collisional regime.<sup>17</sup>

The competition among current paths is determined by the vorticity equation

$$\frac{c^2}{B^2} n m_i \frac{d}{dt} \nabla_{\perp}^2 \Phi = \nabla_{\parallel} J_{\parallel} + \frac{2c}{B} \mathbf{b} \times \boldsymbol{\kappa} \cdot \nabla p, \quad (17)$$

where  $d/dt = \partial/\partial t + \mathbf{v} \cdot \nabla$ ,  $\mathbf{v} = (c/B) \mathbf{b} \times \nabla_{\perp} \Phi$ ,  $\Phi$  is the electrostatic potential,  $\mathbf{B} = B\mathbf{b}$  is the magnetic field,  $\boldsymbol{\kappa} = \mathbf{b} \cdot \nabla \mathbf{b} = -(1/R)\hat{\mathbf{e}}_x$  is the magnetic curvature,  $J_{\parallel}$  is the parallel

current density,  $n = n_e = n_i$  is the particle density, and  $p = nT$  is the pressure. Letting  $(x, y)$  denote the local coordinates in the radial and vertical directions at the outer midplane, we write  $\boldsymbol{\kappa} = -(1/R)\hat{\mathbf{e}}_x$  and  $2\mathbf{b} \times \boldsymbol{\kappa} \cdot \nabla p = \boldsymbol{\kappa} = -(2/R)\nabla_y p \approx -(2p/R a_b)$ , where  $a_b$  is the blob radius.

In the two-point model, the vorticity equations in the two regions are given by

$$\frac{c^2}{B^2} m_i n_1 \left( \frac{\partial}{\partial t} + \mathbf{v} \cdot \nabla \right) \nabla_{\perp}^2 \Phi_1 = \frac{J_{12}}{L_1} - \frac{2c}{BR} \frac{\partial(n_1 T_1)}{\partial y} , \quad (18)$$

$$\frac{c^2}{\epsilon_x^2 B^2} m_i n_2 \left( \frac{\partial}{\partial t} + \mathbf{v} \cdot \nabla \right) \nabla_{\perp}^2 \Phi_2 = \frac{(J_{23} - J_{12})}{L_2} , \quad (19)$$

where

$$J_{12} = \frac{-\sigma_{12}}{L_{12}} (\Phi_2 - \Phi_1) , \quad J_{23} = \sigma'_s \Phi_2 , \quad (20)$$

$\sigma'_s$  is proportional to the sheath conductivity, and  $\epsilon_x \ll 1$  is a ‘‘fanning factor’’ associated with the flux tube geometry near the X-point. Note that the curvature drive term is included only at the midplane, and the sheath current loss term is included only in the divertor region. Since we are assuming the density limit is associated with blobs that are disconnected from the sheaths, we make the approximation  $\Phi_2 \ll \Phi_1$ , so that  $\Phi_2$  drops out of Eq. (18), and Eq. (19) is not needed here. This is justified in the parameter regime where X-point effects are strong and the collisionality is large; in that case the vorticity term on the LHS of Eq. (19) balances the  $J_{12}$  term, and  $\Phi_2 \rightarrow 0$  as  $\epsilon_x \rightarrow 0$ .<sup>30</sup>

There are two blob parameter regimes<sup>19</sup> associated with Eq. (18): (i) the resistive ballooning (RB) regime,<sup>19,31</sup> in which the curvature term is balanced by the vorticity term on the left-hand-side of Eq. (18), and (ii) the resistive X-point (RX) regime,<sup>17,19</sup> in which the curvature term is balanced by the parallel current term,  $J_{12}/L_1$ . The 3D BOUT simulations<sup>6</sup> suggest that the Greenwald density limit may correspond to the RX to RB

transition. Thus, the transition up to the density limit should occur in the RX regime in which

$$J_{12} \approx \frac{\sigma_{12}}{L_{12}} \Phi_1 = \frac{2c}{B} \frac{L_1}{R} \frac{n_1 T_1}{a_b}, \quad (21)$$

where  $\partial p / \partial y \approx n_1 T_1 / a_b$ . The radial blob velocity in this regime is given by  $v_x \approx (c/B)(\Phi_1/a_b)$  with the sign chosen to give an outward drift.

Solving for the potential from Eq. (21) and using the result to obtain  $v_x$ , we obtain

$$\begin{aligned} v_x &= \left( \frac{\rho_{s1}}{a_b} \right)^2 \left( \frac{2L_1 L_{12}}{\rho_{s1} R} \right) \left( \frac{\omega_{pi}^2}{4\pi \Omega_i \sigma_{12}} \right) c_{s1}, \\ &= \left( \frac{\rho_{s1}}{a_b} \right)^2 q \Lambda c_{s1}, \end{aligned} \quad (22)$$

where  $\rho_{s1} = c_{s1} / \Omega_i$ ,  $c_{s1} = (T_1 / m_i)^{1/2}$ ,  $\Omega_i = eB / m_i c$ ,  $\omega_{pi}^2 = 4\pi n_1 e^2 / m_i$ ,  $\sigma_{12} = 2n_1 e^2 / (m_e v_{12})$ ,  $v_{12} = 2.9 \cdot 10^{-6} \lambda_C n_1 / T_2^{3/2}$ ,  $\lambda_C$  is the Coulomb logarithm, and  $q = L_1 / R$  (not to be confused with the heat fluxes  $q_\perp$  and  $q_\parallel$ ). In writing Eq. (22), we have assumed that  $\delta n_1 / n_1 \sim 1$  in the spatial region of large transport, so that the effect of background density on the blob velocity can be neglected. In the second form, we introduce the collisionality parameter

$$\Lambda = \left( \frac{m_e}{m_i} \right)^{1/2} \left( \frac{L_\parallel}{\lambda_e} \right), \quad (23)$$

expressed in terms of the electron mean free path  $\lambda_e = v_{the} / v_e \rightarrow v_{the1} / v_{12}$  and  $L_\parallel \rightarrow L_{12}$  in the two-point model notation. One can show from Eq. (19) that the disconnected blob limit  $\Phi_2 \ll \Phi_1$  used to derive Eq. (22) requires  $\Lambda > \Lambda_{crit} = \min[1, \varepsilon_x (a_b / a_*)^{5/2}]$ , where  $a_* = \rho_s^{4/5} L_\parallel^{2/5} / R^{1/5}$ ; thus,  $\Lambda_{crit} = \varepsilon_x (a_b / a_*)^{5/2}$  for small blobs, and  $\Lambda_{crit} = 1$  for sufficiently large blobs. These regimes have been studied in recent 2D simulations of the two-region model,<sup>30</sup> which have shown good agreement between the numerical results

and the analytic scalings [such as Eq. (22)]. A detailed discussion of the collisionality regimes will be presented elsewhere. One can obtain the sheath-connected blob result (valid at low SOL density) heuristically by setting  $\Lambda = 1$  in Eq. (22). Thus, Eq. (22) shows that the blob speed increases with collisionality as the blob current path disconnects electrically from the sheaths.

Note that in this model all quantities are expressed in terms of the midplane values  $n_1$  and  $T_1$  except for the temperature dependence of the collisionality,  $\nu_e = \nu_{12} \propto n_1 T_2^{-3/2}$ . This choice is not essential, but it models the fact that the collisionality (conductivity) of the colder divertor region determines the parallel current flow to the sheaths.

The perpendicular heat flux is obtained by combining Eqs. (6) and (22) and specifying the packing fraction  $f_b \sim (a_b/L_y) (\tau_b/\Delta\tau) < 1$ , where  $L_y$  is the average poloidal spacing between blobs at a given time and  $\tau_b = a_b/v_x$  is the time for a blob to transit past a fixed radial point and  $\Delta\tau$  is the average “waiting time” between emission of consecutive blobs. The upper limit on the packing fraction is  $f_b = 1$ , corresponding to poloidally-dense and continuous emission of blobs, and in the high-density, high-transport regime, we expect that  $f_b$  is of order unity. This assumption can be tested experimentally, as discussed subsequently. We note that the packing fraction is inversely related to the skewness  $S$  of the blob statistics: at low collisionality the blobs are created infrequently, so  $f_b \ll 1$  and  $S \gg 1$ ; as the edge density and collisionality increase, the blob generation rate increases ( $f_b \rightarrow 1$ ) and  $S$  decreases ( $S \sim 1$ ).

This is a subtle point requiring further explanation. As a matter of semantics (depending on the definition of a “blob”), the  $S \sim 1$  region can be viewed either as a strongly turbulent, blob-free state,<sup>13</sup> or as a state with very close-packed blobs where the particle and heat flux is carried entirely by the blobs (the point of view taken here, because it allows us to specify a functional form for the transport). Both viewpoints are valid if one can show that the “mixing length” estimate and the blob estimate of the radial

transport give the same order of magnitude result. In fact, the two estimates are consistent if one assumes a wave-breaking condition for saturation of the turbulence ( $\omega \sim k \cdot v$ ), implying the following correspondence rule<sup>19</sup>

$$\gamma \rightarrow \frac{v_x}{a_b}, k_{\perp} \rightarrow \frac{1}{a_b}, L_n \rightarrow a_b, \quad (24)$$

which relates the properties of the underlying equilibrium and linear instability to the radial blob velocity and scale size. Here,  $\gamma = \text{Im}[\omega]$  is the growth rate of the instability and  $\mathbf{k}$  is the wavenumber. Then, using mixing length theory we estimate (in Bohm units)  $\tilde{n}/n_0 \sim k_{\perp} \tilde{\Phi}/(\omega L_n)$  and  $\tilde{v}_x \sim k_{\perp} \tilde{\Phi}$  and employ the saturation condition  $\omega \sim k_{\perp} \tilde{v}_{\perp}$ , which implies  $\tilde{\Phi} \sim \omega/k_{\perp}^2$  to obtain  $\Gamma \sim \text{Re}[\tilde{n} \tilde{v}_x^*] \sim n_0 \gamma / (k_{\perp}^2 L_n)$ . At the blob generation zone (where strong turbulence sets in, and the estimate becomes qualitative) we use the correspondence rules to obtain  $\Gamma \sim n_0 \gamma a_b$ . On the other hand, from the blob perspective, we estimate  $\Gamma \sim n_b v_x$  with blob density  $n_b \sim n_0$  and convective blob velocity  $v_x \sim \gamma a_b$  [see Eq. (24)] to obtain the same result as in mixing length theory. Thus, the flux estimate from turbulence (which gives rise to the blobs) is consistent with the blob flux. It is the agreement between the “mixing length” and blob estimates that allows us to apply the latter in the blob creation zone.

A recent paper<sup>13</sup> has studied the turbulent blob (or “avaloid”) scaling near the density limit on the Mega Ampere Spherical Tokamak<sup>32</sup> (MAST) and has two points of agreement with the present model: (i) the turbulent fluctuations (measured by  $\langle J_{\text{sat}} \rangle$ ) increase with  $n/n_G$  (also seen in Refs. 10,11, and 25), and (ii) the skewness decreases from about 3 to 1 as  $n/n_G \rightarrow 1$ , suggesting that the blobs are more tightly packed near the density limit. As just discussed, in the limit of  $f_b \sim 1 \sim S$  it is difficult to distinguish blobs from the general turbulent background. In Ref. 13, avaloids are *defined* to be blobs with amplitudes ( $\langle J_{\text{sat}} \rangle$ ) greater than 2.5 times the standard deviation  $\sigma$ , and the point of view is taken that blobs (avaloids) cease to play a significant transport role as  $S \rightarrow 1$ . Here, we do not impose an amplitude threshold on what constitutes a “blob” and use the blob

model as a semi-quantitative means to estimate the scaling of the turbulent transport even as  $S \rightarrow 1$ .

Making use of the approximations just discussed, we obtain

$$q_{\perp 1} = \left( \frac{\rho_{s1}}{a_b} \right)^2 q \Lambda n_1 T_1 c_{s1} . \quad (25)$$

Note that this heat flux is proportional to the product of parameters characterizing the pressure-weighted MHD curvature ( $n_1 T_1 q$ ) and the collisionality ( $\Lambda$ ). The scaling of the perpendicular heat flux on the SOL density and temperature also depends on the scaling of blob size  $a_b$  with gyroradius  $\rho_s$ . If one assumes that  $a_b$  is independent of density and temperature, Eq. (25) gives the scaling  $q_{\perp 1} \propto n_1^2 T_1^2 / T_2^{3/2}$ . Thus, in this case  $\mu = 2$ ,  $\nu = 3$  and the perpendicular transport coefficient defined in Sec. II A scales like  $C_{\perp} \propto n_1^2$ . If we assume  $a_b \propto \rho_s$ , Eq. (25) gives the scaling  $\mu = 1$ ,  $\nu = 3$ . The difference between these scalings is important in what follows. We will see that the latter scaling implies that the blob heat transport  $q_{\perp 1}$  increases as the X-point cools, which is essential for thermal instability.

The result that the thermal physics depends on the blob size scaling (which is presently unknown) highlights the need for more detailed analysis of blob statistics in both experiments and simulations. There are three arguments in favor of the blob scaling  $a_b \propto \rho_s$  assumed here: (i) theoretical scaling arguments suggest that the natural scaling of  $a_b$  must be close to  $\rho_s$ ; (ii) the magnetic field dependence of this scaling has been demonstrated on the LAPD experiment,<sup>33</sup> and (iii) this scaling yields a B-field dependence of the transport which is qualitatively consistent with the simulations in Ref. 6. We also note that the temperature dependence of the scaling  $a_b \propto \rho_s$  has the property that the blob size *decreases* as the SOL cools, which facilitates the transition from the RX to RB blob transport scaling at high collisionality, as observed in the BOUT simulations.<sup>6</sup>

With regard to point (i), we note that the only perpendicular scale length in the problem is  $\rho_s$  and the parallel scales are  $L_{\parallel}$  (or  $R = L_{\parallel}/q$ ) and  $\lambda_{ei}$ . On dimensional grounds, one expects  $a_b \sim \rho_s^{1-p-s} L_{\parallel}^p \lambda_{ei}^s$ , but  $p \ll 1$  and  $s \ll 1$  are necessary to get a “reasonable” perpendicular scale size for the blob.

The magnetic field scaling of the transport in our model [point (iii)] is estimated as follows. From the discussion of quasilinear diffusion, we recall that the effective diffusivity scales as  $D_{\text{eff}} \sim \gamma/k_{\perp}^2 \sim (v_x/a_b) a_b^2 \sim v_x a_b$ , where the blob correspondence rule, Eq. (24), was employed. Using Eq. (22) for the RX-regime blob velocity and assuming that the magnetic field scaling is given by  $a_b \propto \rho_s$ , we find that  $D_{\text{eff}} \sim v_x a_b \sim q/B$  at fixed  $L_{\parallel}$ . This result agrees qualitatively with the trend in the simulations reported in Ref. 6, where it was found that  $D_{\text{eff}}$  increased as  $B$  decreased (at fixed  $q$ ).

The complete scaling of the transport coefficients  $C_{\perp}$  and  $C_{\parallel}$  have the following forms for the blob model described here

$$C_{\perp} = \frac{q_{\perp 1}|_{T_r}}{q_{\perp \text{core}}} = \frac{q \Lambda n_1 c_s T_r}{q_{\perp \text{core}}} \left( \frac{\rho_s}{a_b} \right)^2 \propto \frac{n_1^2}{T_r^{1/2}} \left( \frac{\rho_s}{a_b} \right)^2, \quad (26)$$

$$C_{\parallel} = \frac{q_{23}|_{T_r}}{q_{\perp \text{core}}} \frac{L_{\perp}}{L_{\parallel}} = \frac{\gamma_s n_2 c_s T_r}{q_{\perp \text{core}}} \frac{L_{\perp}}{L_{\parallel}} \propto n_2 T_r^{3/2}, \quad (27)$$

where  $c_s$ ,  $\rho_s$  and  $\Lambda$  are evaluated at the reference temperature and  $T_r$  is defined in Eq. (10). The important point is that both transport coefficients increase with SOL density.

Finally, we estimate the characteristic quantities in the blob model for typical C-Mod parameters ( $B = 5$  T,  $a = 0.22$  m,  $R = 0.85$  m,  $L_1 = L_2 = L_{12} = 8.5$  m) near the density limit ( $\Gamma_{\perp \text{core}} = 2 \times 10^{17}$  cm<sup>-2</sup> s<sup>-1</sup>,  $T_{\text{edge}} = 15$  eV  $\Rightarrow q_{\perp \text{core}} = 3 \times 10^{18}$  eV cm<sup>-2</sup> s<sup>-1</sup>) with  $n_1 = 6 \times 10^{13}$  cm<sup>-3</sup>,  $n_2 = 1.2 \times 10^{14}$  cm<sup>-3</sup> and a blob size (half-width at half-maximum) of  $a_b = 0.5$  cm. For these parameters, we obtain the following estimates: the reference temperature  $T_r = 20$  eV and transport coefficients  $C_{\perp} = 0.1$ ,  $C_{\parallel} = 7.1$ , and  $\xi =$

0.32. Scaled parameters of interest are: the collisionality parameter  $\Lambda = 2.3 (T_r/T_1)^{1/2} (T_r/T_2)^{3/2}$ , the blob size in gyroradii,  $a_b/\rho_s \sim 40 (T_r/T_1)^{1/2}$ , and the blob speed  $v_x(\text{cm/s}) = 0.5 \times 10^5 (T_r/T_2)^{3/2}$ , where the scaling  $a_b/\rho_s \sim \text{const.}$  was assumed in computing  $v_x$ . These results are consistent with the assumption that C-Mod is in the collisional (disconnected) blob regime near the density limit, and the estimated blob velocity is in reasonable agreement with the measured values. Here,  $T_1$  and  $T_2$  are obtained by solving Eqs. (28) and (29) as described in the next section.

### III. Solutions for general scaling

In this section, we apply the two-point SOL energy balance model given by Eqs. (11) and (12) to solve for the thermal equilibrium and the dynamic response of the SOL temperature to cooling by blob heat convection. In deriving the model in Sec. II A, we assumed an arbitrary scaling of the blob transport term, and the scaling was motivated in Sec II B by an analysis of the “sheath-disconnected” blob model, valid for high collisionality. Here, we return to the analysis of the general scaling to illustrate the physical interpretation of the SOL density limit.

#### A. Thermal equilibrium and stability

The thermal equilibrium is determined by the equations for steady-state heat balance in the divertor region and the global SOL

$$F_2 \equiv T_2^{5/2}(T_1 - T_2) + C_{\parallel}(\xi T_1^{3/2} - T_2^{3/2}) = 0 \quad , \quad (28)$$

$$F_{\text{SOL}} \equiv 1 - C_{\perp} \frac{T_1^{\mu}}{T_2^{\nu/2}} - C_{\parallel} T_2^{3/2} = 0 \quad , \quad (29)$$

where  $F_{\text{SOL}}(T_1, T_2) = F_1 + F_2$ , the temperatures are dimensionless [normalized to the reference temperature in Eq. (10)], and the densities have been absorbed into the coefficients,  $C_{\perp} \propto n_1^2$  and  $C_{\parallel} \propto n_2$ .

A numerical solution of Eqs. (28) and (29) for fixed  $C_{\parallel}$  gives the curves of  $T_1$  and  $T_2$  vs  $C_{\perp}$  shown in Fig. 2 and the normalized heat fluxes  $Q_{\perp}$  and  $Q_{\parallel}$  [defined in Eq. (15)] vs  $C_{\perp}$  shown in Fig. 3. For fixed  $C_{\parallel}$  and  $\xi$ , and with values of the perpendicular heat flux exponents satisfying

$$\nu > 2\mu \quad (30)$$

(derived subsequently), the thermal equilibrium problem has two non-zero solutions for  $(T_1, T_2)$  provided that  $C_{\perp}$  is smaller than a critical value ( $C_{\perp} = C_{\perp}^*$ ) defined by the merger of the two roots and indicated by the vertical dotted line in Figs. 2 and 3. Above this critical value, there are no real equilibrium solutions. Thus, this model exhibits a classic “fold catastrophe” corresponding to a limit on the allowed perpendicular convection; the mathematical form of this model is similar to some density limit theories based on radiative cooling which also exhibit catastrophes (see Ref. 2 for a review and Ref. 22 for a relevant example). Here, the convective limit corresponds to a limit on the midplane SOL density,  $n_1 < n_1^*$ , when the blob physics in Sec. II B is taken into account.

The transport properties of the two roots are illustrated in Fig. 3. Except near the root merger point, the “warm X-point” (high-temperature) root is characterized by larger parallel heat flow ( $Q_{\parallel} > Q_{\perp}$ ) whereas the “cold X-point” (lower temperature) root has larger perpendicular heat flow ( $Q_{\perp} > Q_{\parallel}$ ). We will show in what follows that the high-T root is thermally stable and is therefore physically observable, whereas the low-T root is thermally unstable. The model solution shows that parallel heat transport is stabilizing and perpendicular heat transport is destabilizing. Also in agreement with the experiment,<sup>1,10,11</sup> the model predicts that the density limit occurs after  $Q_{\perp}$  exceeds  $Q_{\parallel}$  for the physically observable root (see Fig. 3). This agreement is vividly illustrated by a plot of the power flows for more recent C-Mod data (see Fig. 18 in Ref. 11), which should be compared with the physically observable “warm X-point” root in Fig. 3. This comparison is discussed in more detail in Sec. IV.

When Eq. (30) is violated, the SOL thermal equilibrium problem has only one root for all values of  $C_{\perp}$  (at fixed  $C_{\parallel}$  and  $\xi$ ), and this root is stable to thermal perturbations. The SOL plasma simply cools as the convection becomes stronger.

We can solve the problem analytically in special limits to shed some light on the numerical results. We note that the divertor energy conservation equation, Eq. (28), has a simple solution of the form  $T_1/T_2 = \varpi$  when  $C_{\parallel} \ll 1$  (with  $\varpi = 1$ ) or when  $C_{\parallel} \gg 1$  (with  $\varpi = \xi^{-2/3}$ ). Substituting the solution for  $T_1$  into Eq. (29) gives an equation for  $T_2$  of the form

$$F_{\text{SOL}}(T_2) \equiv 1 - C_{\perp} \varpi^{\mu} T_2^{\mu - \nu/2} - C_{\parallel} T_2^{3/2} = 0 \quad . \quad (31)$$

The three terms in this equation represent the core heat source, cooling by perpendicular blob convection, and parallel heat flow to the sheaths, respectively. Here,  $C_{\perp}$  and  $C_{\parallel}$  are both positive and we use the maximal ordering  $C_{\perp} \sim C_{\parallel}$ . As shown in Fig. 2, for a fixed value of  $C_{\parallel}$  and under certain conditions which we now derive, Eq. (31) will have two solutions and an equilibrium limit on  $C_{\perp}$ . To obtain the critical values of  $T_2$  and  $C_{\perp}$ , we first solve for  $C_{\perp} = C_{\perp}(T_2, C_{\parallel})$

$$\varpi^{\mu} C_{\perp} = T_2^{(\nu - 2\mu)/2} - C_{\parallel} T_2^{(\nu - 2\mu + 3)/2} \quad . \quad (32)$$

Setting  $\partial C_{\perp} / \partial T_2 = 0$  and solving for the temperature  $T_2^*$  at the root merger point, we obtain

$$T_2^* = \left( \left( \frac{\nu - 2\mu}{\nu - 2\mu + 3} \right) \frac{1}{C_{\parallel}} \right)^{2/3} \quad . \quad (33)$$

Demanding that  $T_2^*$  be real and non-zero for a physical equilibrium solution, we obtain the simple condition on the temperature scalings given in Eq. (30), viz.  $\nu > 2\mu$ , to obtain an equilibrium limit. The limiting value  $C_{\perp}^*$  is then obtained by substituting the solution for  $T_2^*$  into Eq. (32) and collecting terms. We can write the equilibrium limit as

$$\varpi^\mu C_\perp^* C_\parallel^k = \frac{k^k}{(k+1)^{k+1}} \quad , \quad (34)$$

where  $k = (\nu - 2\mu)/3$ ,  $C_\perp \propto n_1^2$  and  $C_\parallel \propto n_2$ .

The SOL density limit condition in Eq. (30) requires that the temperature dependence in the denominator of  $q_\perp$  be stronger than in the numerator. This condition ensures that *the radial convective heat flux increases as the X-point cools*. This is the physical mechanism behind the density limit in this paper. It is obviously related to thermal instability, because the increased radial heat flux will further cool the X-point, leading to rapid cooling of the SOL. When Eq. (30) is satisfied, the thermal equilibrium solution has the form shown in Fig. 2 with the root merger point given by Eqs. (33) and (34) for  $C_\parallel$  large or small.

Figure 4 illustrates the equilibrium boundary in  $(C_\perp, C_\parallel)$  space for our base case,  $\mu = 1$ ,  $\nu = 3$ , and  $\xi = 0.5$ . The solid line denotes the root merger point obtained by numerical solution of Eqs. (28) and (29), and the dotted lines indicate the analytic solutions in the small- and large- $C_\parallel$  limits given by Eq. (34). The analytic and numerical solutions agree in the two asymptotic limits. Thermal equilibrium exists below the indicated curve. Given the density scalings of the transport coefficients, this boundary also implies a limit on the SOL densities  $n_1$  and  $n_2$  to maintain thermal equilibrium.

One can easily demonstrate the connection between this equilibrium limit and thermal instability. Using our analytic equilibrium solution with  $T_1/T_2 = \varpi$  and assuming the time-dependence  $\delta T \sim e^{\gamma t}$ , it is straightforward to obtain a quadratic dispersion relation for the thermal instability growth rate  $\gamma$  from the perturbed versions of Eqs. (11) and (12). Here, we display the result near marginal stability ( $\gamma \rightarrow 0$ ) where the  $\gamma^2$  term can be neglected. In this limit, the perturbed result  $\delta T_1 = \varpi \delta T_2$  holds and one obtains

$$\begin{aligned}
(\varpi\tau_{E1} + \tau_{E2})\gamma\delta T_2 &= \frac{\partial F_{\text{SOL}}}{\partial T_2} \delta T_2 \\
&= \left( \left( \frac{\nu - 2\mu}{2} \right) \frac{C_{\perp}}{T_2^{\nu/2 - \mu + 1}} - \frac{3}{2} C_{\parallel} T_2^{1/2} \right) \delta T_2, \quad (35) \\
&= \frac{3}{2} \frac{k}{T_2} \left( 1 - \left( \frac{T_2}{T_2^*} \right)^{3/2} \right).
\end{aligned}$$

Equation (35) shows that *perpendicular heat convection is destabilizing when  $\nu > 2\mu$* , and that parallel convection is stabilizing. The last form of Eq. (35) uses Eqs. (33) and (34) to show that  $\gamma > 0$  for the low-T root,  $\gamma < 0$  for the high-T root, and  $\gamma = 0$  at the critical point.

Thus, this model confirms the picture that: (1) at low collisionality, SOL heat transport is mainly along the field lines and a higher-temperature (warm X-point) root is obtained which is thermally stable; (2) at high collisionality, the heat transport is mainly across the field, e.g. due to blob convection, and a lower temperature (cold X-point) root is obtained which is thermally unstable. The merger point between the two roots gives the equilibrium limit on SOL density and collisionality, and this limit is also the marginal stability point. It can be shown that these properties hold for the complete model without approximations.

## B. Thermal collapse

The above analysis can be extended to describe the thermal evolution of the SOL in cases where the thermal equilibrium is unstable or does not exist. To illustrate the dynamics of the system, it is instructive to first examine the function  $F_{\text{SOL}}(T_2)$  for fixed parameters  $C_{\perp}$ ,  $C_{\parallel}$  and  $\xi$ . In Fig. 5 we plot the generalization of Eq. (31) which incorporates the exact (arbitrary  $C_{\parallel}$ ) solution of Eq. (28) for  $T_1$ . When  $k \equiv (\nu - 2\mu)/3 > 0$ , the function  $F_{\text{SOL}}(T_2)$  is a parabola, and the condition  $C_{\perp} < C_{\perp}^*$  [see Eq. (34)] ensures that the maximum of  $F_{\text{SOL}}$  [=  $\max(F_{\text{SOL}})$ ] is positive. Under these conditions, the equation  $F_{\text{SOL}}(T_2) = 0$  has low- and high-temperature roots, as discussed previously.

Based on the near-marginal stability analysis of the previous section, we can sketch the direction of motion expected for the SOL: the system moves away from the thermally unstable low-T root, and it moves towards the stable high-T root, as indicated by the arrows in the figure. When  $C_{\perp} > C_{\perp}^*$ ,  $\max(F_{\text{SOL}}) < 0$  and there are no roots. The arrangement shown in Fig. 5 of one stable and one unstable root that merge for a critical value of the control parameter (here,  $C_{\perp}$ ) is referred to by mathematicians as the “fold catastrophe”. When  $k < 0$ , the function  $F_{\text{SOL}}(T_2)$  is a straight line and there is one stable root for each value of the control parameter; thus, there is no equilibrium limit and no thermal instability in this case.

This picture of the thermal evolution of the SOL is confirmed by integration of the time-dependent equations (11) and (12). In Fig. 6 we show a plot of trajectories in the  $(T_1, T_2)$  phase plane for a case with  $k > 0$  and  $C_{\perp} \leq C_{\perp}^*$ . In this case all initial conditions are first attracted to a line, then flow along the line to either the stable high-T root or to  $(0,0)$ . Thus, these two points are attractors for the high- and low-temperature initial conditions, respectively. The trajectories in Fig. 6 show that approximate steady-state is first established in the divertor region [satisfying Eq. (28)] and then on a slower time scale the system evolves towards global heat balance [satisfying Eq. (29)] along the line shown in the figure. For  $k > 0$  and  $C_{\perp} > C_{\perp}^*$  (not shown) all initial conditions flow along the line to  $(0,0)$ . Thermal equilibrium is not possible in this case due to the destabilizing radial heat convection, and thermal collapse of the SOL is the only possible outcome.

A time-asymptotic ( $t \rightarrow \infty$ ) solution of Eqs. (11) and (12) sheds further light on the thermal collapse. To study the behavior as  $(T_1, T_2) \rightarrow (0, 0)$ , we neglect the terms with the highest powers of  $T$  and consider the case  $T_1 \ll T_2$ , so that Eqs. (11) and (12) reduce to:

$$1 = C_{\perp} \frac{T_1^{\mu}}{T_2^{\nu/2}}, \quad \tau_2 \frac{\partial T_2}{\partial t} = -C_{\parallel} T_2^{3/2}, \quad (36)$$

where  $\tau_2 = \tau_{E2} (L_2/L_1)$ . In this limit, perpendicular heat convection is the main cooling mechanism in the midplane, and parallel heat losses to the sheath cool the divertor region. Using the ansatz,  $T_j = A_j t^{\alpha_j}$  for  $j = 1, 2$  with  $A_j$  and  $\alpha_j$  constants to be determined, we obtain the asymptotic solution

$$T_1 = \frac{1}{C_{\perp}^{1/\mu}} \left( \frac{2\tau_2}{C_{\parallel}} \right)^{\nu/\mu} \frac{1}{t^{\nu/\mu}}, \quad T_2 = \left( \frac{2\tau_2}{C_{\parallel}} \right)^2 \frac{1}{t^2}. \quad (37)$$

The neglected terms in Eqs. (11) and (12) are small if  $\nu, \mu > 0$  and satisfy the condition (30) for two roots, viz.  $k > 0$ . This condition insures that  $T_1 \ll T_2$  as  $t \rightarrow \infty$  [see Eq. (37)], consistent with our assumptions. This solution verifies that  $(0, 0)$  is an attractor of the non-equilibrium system as  $t \rightarrow \infty$  when perpendicular heat convection is important.

Finally, in the single root case ( $k < 0$ ), the numerical solution of the trajectory equations (not shown) demonstrates that there is a single stable attractor in the  $(T_1, T_2)$  phase plane, and all initial conditions evolve to this attractor. Thus, dynamical thermal collapse cannot occur in this case.

#### IV. Comparison with the C-Mod experiment

In this section, we discuss the points of agreement between the present model and the experimental data on C-Mod. It will be shown that our calculation provides a simple framework for interpreting many of the recent observations.

The blob model in its original form provided a mechanism for ballistic radial particle and heat transport across the far SOL and interaction with the wall.<sup>15,16</sup> This idea is widely accepted as the most plausible explanation for the observed intermittent transport and two-scale density profile on C-Mod<sup>34,35</sup> and other tokamaks.<sup>35-38</sup> Under conditions when the neutral density in the far SOL is sufficiently high, the plasma blobs can be sustained by local ionization,<sup>16</sup> resulting in a large particle flux to the main chamber wall. This “main chamber recycling” regime was first identified on C-Mod.<sup>34</sup>

Later theoretical work addressed the problem of blob creation and propagation in the near SOL. Both theory<sup>17-19</sup> and simulations<sup>6,17</sup> suggest that the blob transport in the near SOL increases with the collisionality  $\Lambda$  (Sec. II B). For example, the sheath-disconnected (or “RX-mode”<sup>19</sup>) blob model gives Eq. (22) for the blob velocity, which implies an average radial velocity  $v_{\text{eff}} = f_b v_{x,\text{blob}} \propto \Lambda$ .

The choice of blob regime, and thus collisionality dependence, is an important input to our thermal equilibrium and stability model. Another input was the assumed scaling  $a_b \propto \rho_s$ , which has not yet been verified by experimental data but is supported by the arguments given in Sec. II B. With these two assumptions, we obtained the temperature scaling  $\mu = 1$ ,  $\nu = 3$  which determined the equilibrium and stability boundaries computed in this paper. Regarding collisionality, it should be emphasized that the edge density limit discussed here and observed experimentally is caused by the effects of collisionality in the plasma edge and *near SOL*. We assume that in the *far SOL* the blob transport is entirely ballistic: the energy carried by blobs is guaranteed to be lost from the core and the details (e.g. blob regime) do not play a role in establishing the density limit. Recent measurements on C-Mod and DIII-D confirm that collisionality is not an important parameter in determining the net radial transport in the far SOL.<sup>35</sup>

The predictions of our thermal equilibrium and stability model, incorporating these recent developments in blob theory, is consistent with recent experimental investigations<sup>1,10,11</sup> of the density limit on C-Mod. It was found that cross-field heat transport increases strongly with collisionality and eventually dominates parallel heat transport, leading to a convective density limit. For a given collisionality, the SOL heat transport has two spatial regions: (1) a hot inner region where the collisionality is low and the power  $P_{\text{SOL}}$  flowing to the SOL is lost mainly by parallel heat transport,  $q_{\parallel} A_{\parallel}$ ; and (2) a cooler outer region where the collisionality is high,  $P_{\text{SOL}}$  is lost mainly by cross-field heat transport,  $q_{\perp} A_{\perp}$ , and the density and pressure profiles are flat. In the original experiments,<sup>10</sup> it was shown that the boundary between these regions moved inwards as

the collisionality increased, reaching the separatrix for  $n_e/n_G \approx 1$  so that the entire SOL is in the collisional regime at the density limit. It was found that the condition  $q_\perp A_\perp > q_\parallel A_\parallel$  (implying  $Q_\perp > Q_\parallel$  in the present model) is satisfied in the near SOL for  $n_e/n_G > 0.43$  (see Fig. 5 of Ref. 10). Thus, the dominance of the perpendicular heat transport just outside the separatrix is a characteristic feature of the density limit on C-Mod. This is also obtained in our model calculations, as shown by the crossing of the solid curves ( $Q_\perp > Q_\parallel$ ) for the physically-observable “warm X-point” root in Fig. 3. This is one of the most important points of agreement between our model and the experiment.

In more recent experiments,<sup>11</sup> this conclusion was extended to a greater range of discharge conditions, and the power flow data was plotted as a function of  $n_e/n_G$  and the collisionality parameter  $\alpha_d$  [see Figs. 18 (a) and (b) of Ref. 11]. For future reference, the two collisionality parameters used in Ref. 11 (based on the work of Rodgers, Drake and Zeiler<sup>5</sup> and Scott<sup>4</sup>) are related to our parameter  $\Lambda$  by

$$\alpha_d = \frac{1}{8\pi} \left( \frac{2R}{a_b} \right)^{1/4} \left( \frac{1}{q\Lambda} \right)^{1/2}, \quad C_0 = \left( \frac{R}{a_b} \right) q\Lambda, \quad (38)$$

where the approximation  $L_\perp \approx a_b$  was used. Note that  $C_0 \propto q\Lambda$  is analogous to the parameter  $C_\perp$  used in the present model, and  $\alpha_d \propto 1/(q\Lambda)^{1/2}$ . Thus, a comparison of Fig. 18 of Ref. 11 with the physically-observable “warm X-point” root in Fig. 3 shows remarkable qualitative agreement between the heat flow predictions of our model and the experimental measurements. The numerical simulation codes<sup>4-6</sup> and the analytic blob model calculations suggest that turbulent cross-field transport increases with collisionality and leads to the C-Mod density limit.

The idea that the turbulent transport is mediated by blobs is also supported by recent observations<sup>24,25</sup> using the C-Mod gas puff imaging diagnostic.<sup>23</sup> It is observed that the edge turbulence level near the separatrix increases,<sup>11,24,25</sup> and the blob birth zone moves inward, as the density is raised and the collisionality increases. The blob birth

zone moves inside the separatrix for  $n_e/n_G > 0.7$  [e.g. see Fig. 5 in Ref. 25]. Measurements also show that the temperature inside the separatrix cools and the temperature gradient decreases as  $n_e/n_G \rightarrow 1$ . As pointed out in Ref. 24, the C-Mod data is consistent with the idea that blobs are born in the steep gradient region (which moves inwards past the separatrix with increasing edge collisionality), not at the transition from open to closed field lines.

As a final check, we carry out estimates of important physical quantities using typical C-Mod parameters for the physically-observable high-T root to show that the model is consistent and relevant to the experiment. As pointed out in Sec. II B, the blob speed  $v_x \sim 10^5$  cm/s if  $a_b/\rho_s \sim \text{const.}$  and (dimensionless)  $T_2 \sim 1$  is assumed, which is reasonably consistent with the measured velocities. The transport coefficients for typical C-Mod parameters are  $C_\perp = 0.1$ ,  $C_\parallel = 7.1$ , which imply an equilibrium limit of  $C_\perp^* = 0.25$  using Eq. (34) with  $\mu = 1$ ,  $\nu = 3$ . Thus, the system is close to the theoretical density limit ( $C_\perp \sim C_\perp^*$ ), implying that the model is relevant to C-Mod experiments. We also estimated the collisionality parameter to be  $\Lambda \sim 2$  at low values of  $C_\perp$ , and  $\Lambda$  increases with  $C_\perp$  ( $\propto n_1^2$ ) because the normalized  $T_1$  and  $T_2$  decrease due to convective heat transport (see Fig. 2). This implies that blobs in the near SOL are disconnected from the sheaths ( $\Lambda > \Lambda_{\text{crit}}$ ) for typical C-Mod parameters, as assumed in the derivation of the blob model. Thus, we conclude that the thermal equilibrium model including blob convection is internally consistent and in reasonable qualitative agreement with both experimental observations<sup>1,10,11,25</sup> and recent density limit simulations using 3D turbulence codes.<sup>4-6</sup> Given the many approximations and the 0D nature of the model, we cannot expect to make more quantitative comparisons with the experiment.

In summary, the experimental work and the model discussed in the present paper support the following picture of the convective density limit in C-Mod. The density limit is caused by edge and SOL cooling resulting from turbulence-induced cross-field blob convection. Both the blob source rate and the velocity of radial motion increase with

disconnection from the sheaths and hence with collisionality. The X-points play an important role in enhancing the disconnection (facilitating current loop closure by perpendicular currents across the thin fanned flux tubes) and in blurring the boundary between open and closed field lines. This permits blobs to be born inside the nominal separatrix position and to interact with the nominal core plasma. (However, the phenomenon does not require X-points, as the RX-regime of blob transport assumed here goes over to the resistive ballooning (RB) regime at high collisionality, which is independent of X-points and has even faster cross-field transport.<sup>19</sup>) As the cooling moves inwards, the core current channel is eventually affected and a conventional MHD disruption occurs. In this paper, we have not modeled the penetration of the blob convection inside the separatrix, but have simply used SOL thermal collapse as a measure of the approach to the density limit.

## V. Summary and Conclusion

In this paper, we have described a two-point model of SOL energy balance including radial heat convection  $q_{\perp}$  (Sec. II) and demonstrated the existence of a convective density limit (Sec. III) to avoid thermal collapse of the SOL. The edge-density limit is caused by the collisionality dependence of the cross-field heat convection. Using a general scaling of  $q_{\perp}$  with the temperatures in the midplane and X-point regions [see Eq. (7)], we derived a general condition for thermal instability, Eq. (30), and an expression for the equilibrium boundary, Eq. (34). The thermal instability is associated with X-point cooling and is analogous to an X-point MARFE with radiation replaced by cross-field heat convection. The instability requires that the radial convective heat flux increase as the X-point cools. As described in Sec. IV, several features of the model are qualitatively consistent with Alcator C-Mod data.

A specific mechanism for the radial heat transport was discussed in Sec. II B, viz. turbulent blob convection. A dimensional analysis of the vorticity equation suggests that

blobs in the RX-mode turbulence regime, which are electrically and thermally disconnected from the sheaths, have the correct scaling for thermal instability under the reasonable (but not yet confirmed) assumption that the blob size scales with gyroradius ( $a_b \propto \rho_s$ ). With this assumption, we obtained the temperature scaling  $\mu = 1$ ,  $\nu = 3$ , which satisfies the condition [Eq. (30)] for thermal collapse at sufficiently large  $q_{\perp}$ . Another consequence of this scaling is that the radial transport has a B-field scaling ( $D_{\text{eff}} \sim q/B$ ) that is qualitatively consistent with previous simulations<sup>6</sup> [see Sec. II B]. Statistical studies of blob creation and investigations of theoretical scaling of  $v_x$  are under way in both experiments and turbulence simulations and should provide a test of the present model.

It is straightforward to show that the equilibrium limit derived in this paper is actually a limit on the edge density. The equilibrium limit is defined to be  $C_{\perp} \leq C_{\perp}^*$  for  $\nu > 2\mu$ , where  $C_{\perp}^* \sim 1$  by Eq. (34) for values of  $C_{\parallel}$  not too different from unity. The inequality  $C_{\perp} \leq 1$  can be rewritten as  $q_{\perp r} \leq q_{\perp \text{core}}$ , where  $q_{\perp r}$  is the cross-field heat flux in the SOL evaluated at the reference temperature ( $T_1, T_2 \rightarrow T_r$ ). We rewrite this condition as

$$f_b n_1 T_r v_{\perp, \text{blob}} \leq q_{\perp \text{core}} \quad , \quad (39)$$

where  $f_b$  is the blob packing fraction and  $f_b v_{\perp, \text{blob}} = v_{\text{eff}}$  is an effective mean radial velocity. The velocity  $v_{\perp, \text{blob}}$  has an explicit dependence on  $n_1$  in the RX-blob regime [see Eq. (22)] and  $f_b$  may have an implicit density dependence, so the LHS of Eq. (39) is a function of the midplane SOL density  $n_1$ . Thus Eq. (39) provides a rough order-of-magnitude analytical estimate of the SOL density limit due to the thermal transport catastrophe. A more precise characterization is obtained by employing the dimensionless parameters  $C_{\perp}$  and  $C_{\parallel}$  in a numerical solution for the density limit boundary, such as shown in Fig. 4.

The present work uses the ideas of turbulence-induced density limits, density-(collisionality-) dependent cooling, and thermal instability of X-points; it combines them with recent theories of three-dimensional blob transport to elucidate and confirm recent insights into the nature of the density limit. Our conclusions are consistent with evidence from recent simulations<sup>4-6</sup> and the C-Mod experiment<sup>10-11</sup> that the turbulent fluxes increase with collisionality [Eq. (25)] and lead to a transport-driven density limit [Figs. 2 - 4]. This model supports the idea that the physical mechanism responsible for the enhanced turbulent transport (and resulting density limit) is the electrical and thermal disconnection of the fluctuations from the divertor.

Finally, it has been noted elsewhere that the C-Mod density limit experiments raise some interesting questions:<sup>1</sup> (i) whether radiation-related phenomena or density-dependent transport are the underlying cause of the density limit, and (ii) whether there is a maximum density independent of atomic processes. The present work suggests that radial heat convection with a sufficiently strong negative temperature scaling can limit the density in toroidal plasmas without invoking radiation, but the role of particle sources such as ionization has not yet been evaluated. Turbulent blob transport is a universal phenomenon and is a likely candidate mechanism for driving the density limit. The present paper has identified conditions for this to occur. This mechanism will occur even in plasmas without impurities, as it relies only on the presence of curvature-driven edge turbulence.

## **Acknowledgements**

We would like to thank M. Greenwald, B. LaBombard, and J. Terry for useful and stimulating discussions on the density limit and C-Mod data. We also thank D. A. Russell for ongoing discussions and collaboration on blob physics which helped motivate this work. This work was supported by the U.S. Department of Energy (DOE) under DOE

Grant No. DE-FG02-97ER54392; however, this support does not constitute an endorsement by the DOE of the views expressed herein.

## References

- <sup>1</sup> M. Greenwald, *Plasma Phys. Control. Fusion* **44**, R27 (2002).
- <sup>2</sup> J. W. Connor, *Theory of Fusion Plasmas: Proceedings of the Joint Varenna-Lausanne International Workshop*, Varenna, August 27-30 2002, p.31 (Società Italiana di Fisica, 2002).
- <sup>3</sup> M. Z. Tokar, *Phys. Rev. Lett.* **91**, 095001 (2003); M. Z. Tokar, F. A. Kelly, and X. Loozen, *Phys. Plasmas* **12**, 052510 (2005).
- <sup>4</sup> B. Scott, *Plasma Phys. Control. Fusion* **39**, 1635 (1997).
- <sup>5</sup> B. N. Rogers, J. F. Drake, and A. Zeiler, *Phys. Rev. Lett.* **81**, 4396 (1998); B. N. Rogers and J. F. Drake, *Phys. Rev. Lett.* **79**, 229 (1997).
- <sup>6</sup> X. Q. Xu, W. M. Nevins, T. D. Rognlien, *et al.*, *Phys. Plasmas* **10**, 1773 (2003).
- <sup>7</sup> K. Borrass, *Nucl. Fusion* **31**, 1035 (1991).
- <sup>8</sup> K. Borrass, R. Schneider, and R. Farengo, *Nucl. Fusion* **37**, 523 (1997).
- <sup>9</sup> I. H. Hutchinson, R. Boivin, F. Bombarda, *et al.*, *Phys. Plasmas* **1**, 1511 (1994).
- <sup>10</sup> B. LaBombard, R. L. Boivin, M. Greenwald, *et al.*, *Phys. Plasmas* **8**, 2107 (2001).
- <sup>11</sup> B. LaBombard, J. W. Hughes, D. Mossessian, M. Greenwald, B. Lipshultz, J. L. Terry, *et al.*, *Nucl. Fusion* **45**, 1658 (2005).
- <sup>12</sup> M. Greenwald, J. L. Terry, S. M. Wolfe, *et al.*, *Nucl. Fusion* **12**, 2199 (1988).
- <sup>13</sup> G. Y. Antar, G. Counsell, and J.-W. Ahn, *Phys. Plasmas* **12**, 082503 (2005).
- <sup>14</sup> D. L. Rudakov, J. A. Boedo, R. A. Moyer, *et al.*, *Nucl. Fusion* **45**, 1589 (2005).
- <sup>15</sup> S. I. Krasheninnikov, *Phys. Lett. A* **283**, 368 (2001).
- <sup>16</sup> D. A. D'Ippolito, J. R. Myra, and S. I. Krasheninnikov, *Phys. Plasmas* **9**, 222 (2002).
- <sup>17</sup> D. A. Russell, D. A. D'Ippolito, J. R. Myra, W. M. Nevins, and X. Q. Xu, *Phys. Rev. Lett.* **93**, 265001 (2004).
- <sup>18</sup> S. I. Krasheninnikov, D. D. Ryutov, and G. Q. Yu, *J. Plasma Fusion Res.* **6**, 139 (2005).
- <sup>19</sup> J. R. Myra and D. A. D'Ippolito, *Phys. Plasmas* **12**, 092511 (2005).
- <sup>20</sup> D. A. D'Ippolito, J. R. Myra, S. I. Krasheninnikov, G. Q. Yu, and A. Yu. Pigarov, *Contrib. Plasma Phys.* **44**, 205 (2004).
- <sup>21</sup> J. R. Myra, D. A. D'Ippolito, S. I. Krasheninnikov, and G. Q. Yu, *Phys. Plasmas* **11**, 4267 (2004).
- <sup>22</sup> P. N. Guzdar, *Phys. Fluids* **27**, 447 (1984).
- <sup>23</sup> S. J. Zweben, D. P. Stotler, J. L. Terry, B. LaBombard, M. Greenwald, *et al.*, *Phys. Plasmas* **9**, 1981 (2002).

- <sup>24</sup> J.L. Terry, S.J. Zweben, K. Hallatchek, B. LaBombard, R. J. Maqueda, *et al.*, Phys. Plasmas **10**, 1739 (2005).
- <sup>25</sup> J.L. Terry, N.P. Basse, I. Cziegler, M. Greenwald, O. Grulke, B. LaBombard, S.J. Zweben, *et al.*, Nucl. Fusion **45**, 1321 (2005).
- <sup>26</sup> D. A. D'Ippolito and J. R. Myra, Phys. Plasmas **10**, 4029 (2003).
- <sup>27</sup> G. Q. Yu and S. I. Krasheninnikov, Phys. Plasmas **10**, 4413 (2003).
- <sup>28</sup> J. R. Myra, D. A. D'Ippolito, X. Q. Xu, and R. H. Cohen, Phys. Plasmas **7**, 2290 (2000) and Phys. Plasmas **7**, 4622 (2000).
- <sup>29</sup> D. Farina, R. Pozzoli, and D. D. Ryutov, Nucl. Fusion **33**, 1315 (1993).
- <sup>30</sup> D. A. Russell, D. A. D'Ippolito, J. R. Myra, Bull. APS **50**, 84 (2005), paper CP1 45.
- <sup>31</sup> O. E. Garcia, N. H. Bian, V. Naulin, A. H. Nielsen, and J. Juul Rasmussen, Phys. Plasmas **12**, 090701 (2005).
- <sup>32</sup> A. Sykes, J.-W. Ahn, and R. Akers, Phys. Plasmas **8**, 2102 (2001).
- <sup>33</sup> T. Carter, Phys. Plasmas **13**, 010701, 2006.
- <sup>34</sup> M. Umansky, S. I. Krasheninnikov, B. LaBombard and J. Terry, Phys. Plasmas **5**, 3373 (1998); B. LaBombard, M. Umansky, R. L. Boivin, *et al.*, Nucl. Fusion **40**, 2041 (2000).
- <sup>35</sup> B. Lipschultz, D. Whyte, and B. LaBombard, Plasma Phys. Control. Fusion **47**, 1559 (2005).
- <sup>36</sup> G. Y. Antar, P. Devynck, X. Garbet, and S. C. Luckhardt, Phys. Plasmas **8**, 1612 (2001).
- <sup>37</sup> J. Neuhauser, D. Coster, H. U. Fahrback, J. C. Fuchs, *et al.*, Plasma Phys. Control. Fusion **44**, 855 (2002).
- <sup>38</sup> J. A. Boedo, D. Rudakov, R. Moyer, S. Krasheninnikov, D. Whyte, *et al.*, Phys. Plasmas **8**, 4826 (2001).

## Figure Captions

Fig. 1 (Color online) Schematic of two self-consistent SOL states: (i) the sheath-connected, hot X-point state, and (ii) the disconnected, cold X-point state. These are described in more detail in the text.

Fig. 2 Midplane temperature  $T_1$  and X-point temperature  $T_2$  vs  $C_{\perp}$  for  $C_{\parallel} = 1.0$ ,  $\xi = 0.5$ ,  $\mu = 1$ , and  $\nu = 3$ . Here  $T$  is normalized to the reference temperature  $T_r$  defined in Eq. (10). Note that there is a warm X-point root (solid lines) and a cold X-point root (dashed lines). The roots merge at a critical value of convection, [see Eq. (33)], and thermal equilibrium does not exist for  $C_{\perp} > C_{\perp}^*$ .

Fig. 3 Dimensionless heat flows  $Q_{\perp}$  and  $Q_{\parallel}$  vs  $C_{\perp}$  for the two roots shown in Fig. 1, which satisfy  $Q_{\perp} + Q_{\parallel} = 1$  for thermal equilibrium. The solid curves denote the “warm X-point” (high-T) root, and the dashed curves the “cold X-point” (low-T) root. At small  $C_{\perp}$ , the high-T root has  $Q_{\parallel} > Q_{\perp}$  and the low-T root has  $Q_{\perp} > Q_{\parallel}$ . For the physically-observable high-T root,  $Q_{\perp}$  exceeds  $Q_{\parallel}$  just before the equilibrium limit is reached, as observed in C-Mod.

Fig. 4 SOL density limit obtained by the numerical solution of Eqs. (27) and (28) (solid line) and by the analytic solution [Eq. (33)] in the small- and large- $C_{\parallel}$  limits (dotted lines) for  $\mu = 1$ ,  $\nu = 3$ , and  $\xi = 0.5$ . Thermal equilibrium exists below the curve. The transport coefficients scale with density as  $C_{\perp} \propto n_1^2$  and  $C_{\parallel} \propto n_2$ .

Fig. 5 Plot of  $F_{\text{SOL}}$  vs  $T_2$  for the parameters  $C_{\parallel} = 1.0$ ,  $C_{\perp} = 0.15$ ,  $\xi = 0.5$ ,  $\mu = 1$ ,  $\nu = 3$ . Note that global energy balance,  $F_{\text{SOL}} = 0$ , has two roots, one stable and one unstable. The evolution of nearby states is indicated schematically by the arrows. The two stable attractors of the dynamical evolution are  $T_1 = T_2 = 0$  and the high-T root (see Fig. 6), so the system exhibits a fold catastrophe.

Fig. 6 Plot of trajectories in the  $(T_1, T_2)$  phase plane with the direction of flow indicated by arrows. The attractors and unstable root are marked by a dot and an  $x$ , respectively. For this case, the parameters are  $C_{\parallel} = 1.0$ ,  $C_{\perp} = 0.2$ ,  $\xi = 0.5$ ,  $\mu = 1$ ,  $\nu = 3$ , and  $\tau_{E1} = 1 = \tau_{E2}$  so that  $C_{\perp} \leq C_{\perp}^* \approx 0.33$ . When  $C_{\perp} \leq C_{\perp}^*$ , all initial conditions are first attracted to a line, then flow along the line to either the stable fixed point or to  $(0,0)$ . For  $C_{\perp} > C_{\perp}^*$  (not shown) all initial conditions flow along the line to  $(0,0)$ .

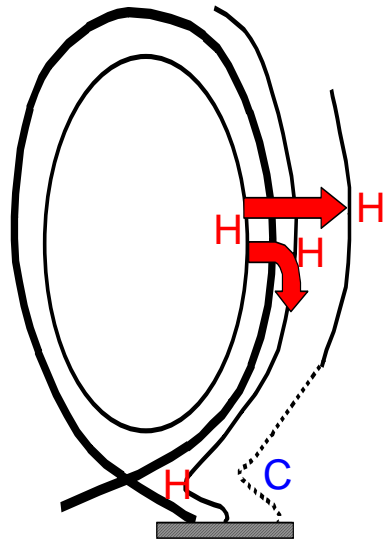


Fig. 1 (Color online) Schematic of two self-consistent SOL states: (i) the sheath-connected, hot X-point state, and (ii) the disconnected, cold X-point state. These are described in more detail in the text.

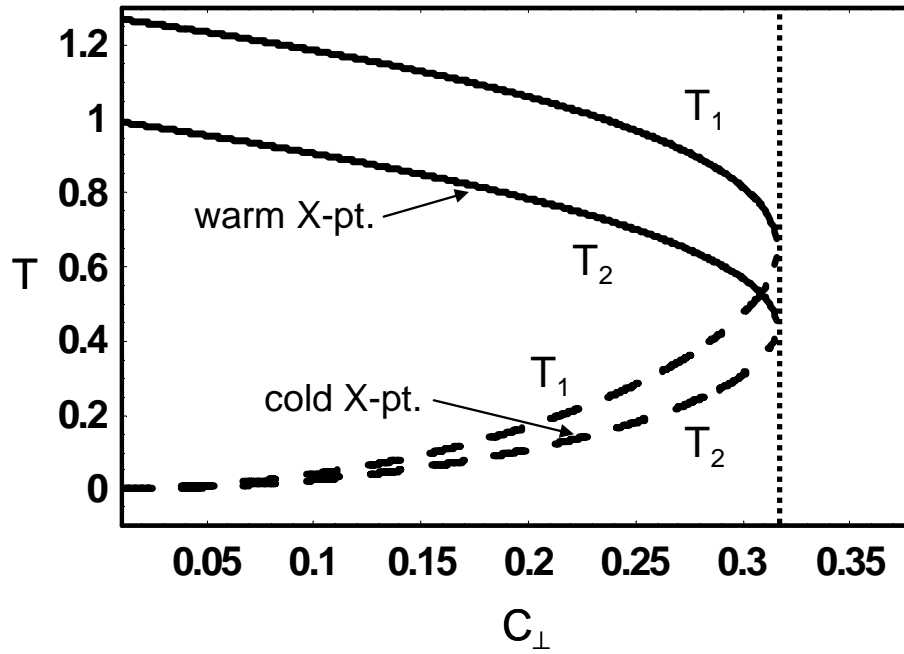


Fig. 2 Midplane temperature  $T_1$  and X-point temperature  $T_2$  vs  $C_{\perp}$  for  $C_{\parallel} = 1.0$ ,  $\xi = 0.5$ ,  $\mu = 1$ , and  $\nu = 3$ . Here  $T$  is normalized to the reference temperature  $T_r$  defined in Eq. (10). Note that there is a hot X-point root (solid lines) and a cold X-point root (dashed lines). The roots merge at a critical value of convection,  $C_{\perp} = C_{\perp}^*$  [see Eq. (34)], and thermal equilibrium does not exist for  $C_{\perp} > C_{\perp}^*$ .

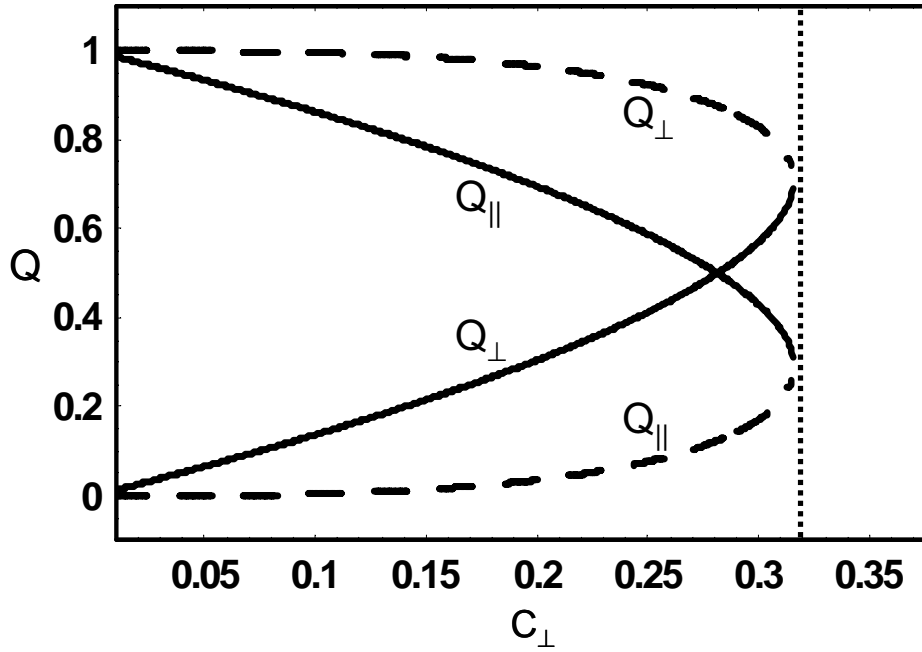


Fig. 3 Dimensionless heat flows  $Q_{\perp}$  and  $Q_{\parallel}$  vs  $C_{\perp}$  for the two roots shown in Fig. 1, which satisfy  $Q_{\perp} + Q_{\parallel} = 1$  for thermal equilibrium. The solid curves denote the “warm X-point” (high-T) root, and the dashed curves the “cold X-point” (low-T) root. At small  $C_{\perp}$ , the high-T root has  $Q_{\parallel} > Q_{\perp}$  and the low-T root has  $Q_{\perp} > Q_{\parallel}$ . For the physically-observable high-T root,  $Q_{\perp}$  exceeds  $Q_{\parallel}$  just before the equilibrium limit is reached, as observed in C-Mod.

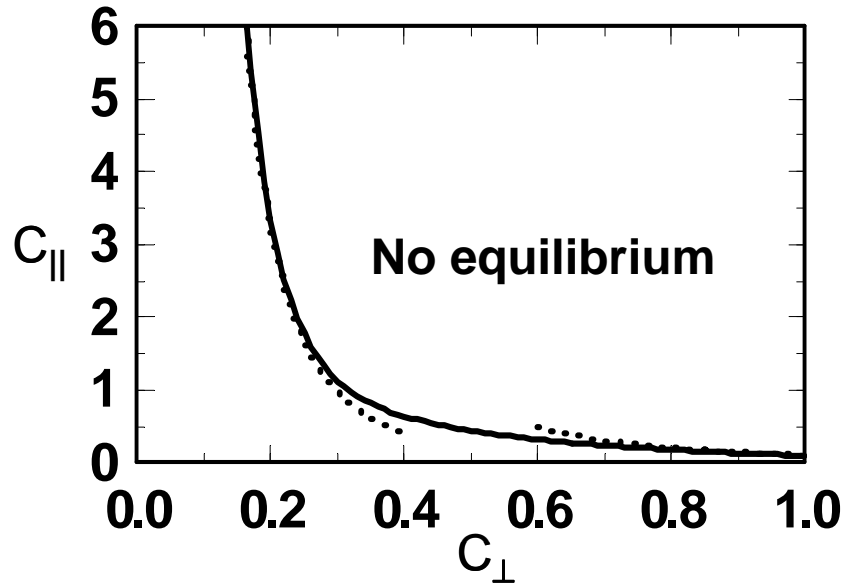


Fig. 4 SOL density limit obtained by the numerical solution of Eqs. (27) and (28) (solid line) and by the analytic solution [Eq. (33)] in the small- and large- $C_{\parallel}$  limits (dotted lines) for  $\mu = 1$ ,  $\nu = 3$ , and  $\xi = 0.5$ . Thermal equilibrium exists below the curve. The transport coefficients scale with density as  $C_{\perp} \propto n_1^2$  and  $C_{\parallel} \propto n_2$ .

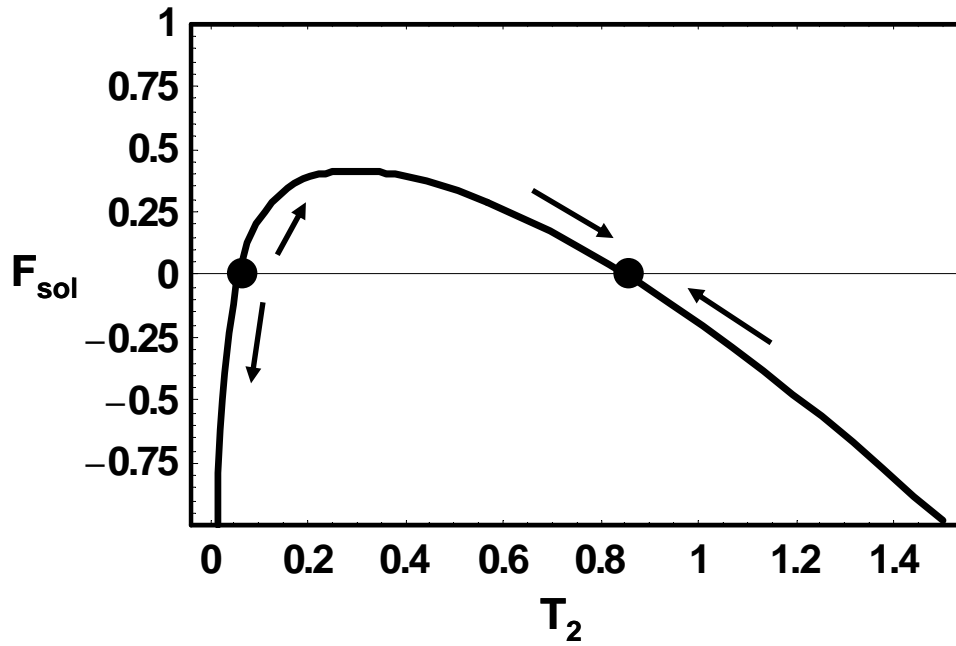


Fig. 5 Plot of  $F_{\text{SOL}}$  vs  $T_2$  for the parameters  $C_{\parallel} = 1.0$ ,  $C_{\perp} = 0.15$ ,  $\xi = 0.5$ ,  $\mu = 1$ ,  $\nu = 3$ . Note that global energy balance,  $F_{\text{SOL}} = 0$ , has two roots, one stable and one unstable, for  $k = (\nu - 2\mu)/3 > 0$ . The evolution of nearby states is indicated by the arrows. The two stable attractors of the dynamical evolution are  $T_1 = T_2 = 0$  and the high- $T$  root (see Fig. 6), so the system exhibits a fold catastrophe.

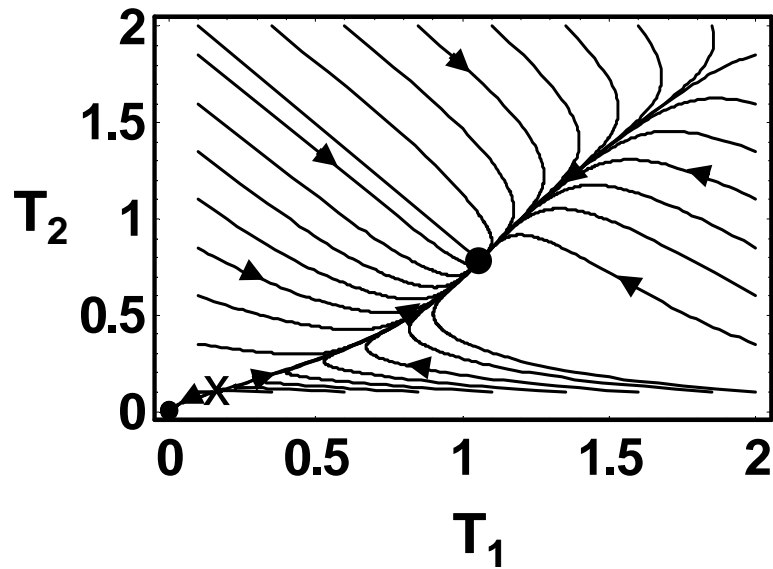


Fig. 6 Plot of trajectories in the  $(T_1, T_2)$  phase plane with the direction of flow indicated by arrows. The attractors and unstable root are marked by a dot and an x, respectively. For this case, the parameters are  $C_{\parallel} = 1.0$ ,  $C_{\perp} = 0.2$ ,  $\xi = 0.5$ ,  $\mu = 1$ ,  $\nu = 3$ , and  $\tau_{E1} = 1 = \tau_{E2}$ , so that  $C_{\perp} \leq C_{\perp}^* \approx 0.33$ . When  $C_{\perp} \leq C_{\perp}^*$ , all initial conditions are first attracted to a line, then flow along the line to either the stable fixed point or to  $(0,0)$ . For  $C_{\perp} > C_{\perp}^*$  (not shown) all initial conditions flow along the line to  $(0,0)$ .